Journal of Power Sources 496 (2021) 229856

Contents lists available at ScienceDirect

Journal of Power Sources

journal homepage: www.elsevier.com/locate/jpowsour

# The apparent capacity decay by kinetic degradation of $LiNi_{0.5}Co_{0.2}Mn_{0.3}O_2$ during cycling under the high upper-limit charging potential

Jiyang Li, Jingxin Huang **, Xiangbang Kong, Jing Zeng, Jinbao Zhao *

*State Key Laboratory of Physical Chemistry of Solid Surfaces, Collaborative Innovation Centre of Chemistry for Energy Materials, State-Province Joint Engineering Laboratory of Power Source Technology for New Energy Vehicle, Engineering Research Center of Electrochemical Technology, Ministry of Education, College of Chemistry and Chemical Engineering, Xiamen University, Xiamen, 361005, PR China*

## HIGHLIGHTS

- Kinetic degradation of $Li^+$ de-/intercalation dominates the capacity decay.
- Reducing current density or increasing operating temperatures can overcome it.
- The electrochemical passivation of the surface structure is a key factor.

## ARTICLE INFO

*Keywords:*
$LiNi_{0.5}Co_{0.2}Mn_{0.3}O_2$
High voltage
Long cycle
Capacity decay
Kinetic degradation

## ABSTRACT

The energy density of $LiNi_{0.5}Co_{0.2}Mn_{0.3}O_2$ (NCM523) can be enhanced by increasing the upper-limit charging potential, but it exhibits a significant "capacity decay" during cycling. Therefore, it is necessary to study the intrinsic mechanism for the performance improvement of high-voltage NCM523. In this work, through combining the intrinsic state-of-charge (SOC) of NCM523 revealed by Raman spectroscopy with the electrochemical characterization, the kinetic degradation of $Li^+$ de-/intercalation is found to be a key factor for the apparent capacity decay of NCM523 under the high upper-limit charging potential (>4.3 V). Meanwhile, the apparent capacity loss can be restored significantly by reducing the current density or increasing the operating temperature. Furthermore, the formation of the electrochemical passivation layer on the surface of NCM523 particles is detected by the surface characterization of high-resolution transmission electron microscopy (HR-TEM) and X-ray photoelectron spectroscopy (XPS), which is proved to be another important factor for the kinetic degradation, besides the particle pulverization of NCM523 and the decomposition products of electrolyte adsorbed on the material surface. Thus, this work can help to rationally improve the electrochemical performance of the high-voltage NCM523.

## 1. Introduction

$LiNi_{0.5}Co_{0.2}Mn_{0.3}O_2$ (NCM523) materials have been widely applied in the commercial lithium ion batteries (LIBs) due to its excellent electrochemical performance and low cost [1–4]. However, the fast development of the electric vehicle market demands the LIBs with higher energy density and longer cycling life. NCM523 can provide more energy density by increasing its upper-limit charging potential (>4.3 V), which exhibits a great potential for meeting the demands of the current fast developing market of electric vehicles [5–7]. However, the capacity of NCM523 will decay rapidly during cycling under high upper-limit charging potentials (>4.3 V), which hinders the potential of the NCM523 materials [8–11]. The possible causes were mainly attributed to the deterioration of the bulk structure of NCM523 and the electrode/electrolyte interface: i) The spinel or rock salt phase formed at the highly delithiated state during charging will cause an anisotropic stress within the NCM523 particle, further leading to the particle pulverization [12–16]. ii) The lithium loss in the continuous growth of the solid electrolyte interphase (SEI) during cycling affects the cycling performance [15]. iii) The adsorption of the decomposition products of electrolyte on the material surface caused by the highly reactive surface oxygen of the $M^{4+}$-O (M = Ni, Co, Mn) will increase the impedance of

---

* Corresponding author.
** Corresponding author.
*E-mail addresses:* huangjingxin@stu.xmu.edu.cn (J. Huang), jbzhao@xmu.edu.cn (J. Zhao).

https://doi.org/10.1016/j.jpowsour.2021.229856
Received 23 November 2020; Received in revised form 2 February 2021; Accepted 26 March 2021

LIBs, thus affecting the capacity retention [17–20]. However, the capacity decay is still serious in the NCM523 half-cell which owns sufficient electrolyte and the nearly infinite lithium inventory. Meanwhile, the contribution of the decomposition products of electrolyte to the impedance growth is still controversial [14,15,20–22]. Therefore, the intrinsic mechanism of the long-cycle capacity decay of NCM523 at the high upper-limit charging potential (>4.3 V) remains poorly understood.

Recently, Kasnatscheew et al. found that most of the apparent capacity loss of $LiNi_{1/3}Co_{1/3}Mn_{1/3}O_2$ (NCM333) in the first cycle (~80–90% coulombic efficiency) is caused by kinetic limitations, which can be recovered reversibly by a constant-potential step at the discharge cut-off potential [23]. Similar results have been reported on the low coulombic efficiency of $LiNi_{0.8}Co_{0.1}Mn_{0.1}O_2$ [24] and $LiNi_{0.80}Co_{0.15}Al_{0.05}O_2$ [25] caused by the kinetic limitations in the first cycle. Therefore, it indicates that the intrinsic kinetic limitation of $Li^+$ de-/intercalation may be a key factor for the long-cycle capacity decay of $LiNi_xCo_yMn_{1-x-y}O_2$ (NCM) materials. This work aims to study the possible factors for the kinetic limitations that lead to the long-cycle capacity decay of NCM523 under the high upper-limit charging potential (>4.3 V) from the aspect of the bulk and surface structure of NCM523.

## 2. Experimental section

### 2.1. Structural characterization

Element and morphology characterization: The elemental composition of NCM523 was confirmed by the inductively coupled plasma atomic emission spectroscopy (ICP-AES) Plasma 1000 (NCS, China). The morphology of NCM523 was characterized by the scanning electron microscope (SEM) S-4800 (Hitachi Corporation, Japan).

Raman spectroscopy measurement: A confocal microscopic Raman spectrometer XploRa (Horiba, Japan) was used. The wavelength of the laser was 532 nm and the laser power was set to as low as ~0.1 mW to avoid damaging the NCM523 samples [26]. The spatial resolution was ~1 μm. In order to avoid the difference in the lithiation degrees between different electrodes and different NCM523 particles in the same electrode, each cycled unit consisted of two parallel half-cells and three Raman spectra were collected randomly from different NCM523 particles of each electrode. Each cycled unit under the same voltage region has the similar cycling performance and the Raman spectra can represent the average degree of structural evolutions for each cycled unit (Fig. S3).

X-ray diffraction (XRD) measurement: The XRD measurements used the Rigaku Miniflex 600 (Rigaku, Japan) with Cu Kα radiation (λ = 0.1544 nm). The operating condition is 40 kV and 15 mA. The data was recorded in the 2θ range between 10° and 90° with a scan rate of 2° $min^{-1}$.

High-resolution transmission electron microscopy (HR-TEM) measurement: Protected by argon atmosphere, the active materials were scraped out from the NCM523 electrodes, dispersed in ethanol and then transferred onto a carbon-supported Cu grid. The HR-TEM images were captured by G2 F30 (Tecnai, USA).

X-ray photoelectron spectroscopy (XPS) measurement: The surface element analysis was conducted by the PHI Quantum-2000 scanning ESCA microprobe.

Treatment of the cycled electrodes: The NCM523 electrodes were disassembled from the cycled half-cells, rinsed with DMC and dried. For the Raman spectroscopy measurements, the NCM523 electrodes after rinsing and drying were sealed in argon atmosphere by a spectral cell. For the XRD measurements, the electrodes were sealed onto the sample slide by polyimide tapes. All of these processes were completed in an argon-filled glove box.

### 2.2. Electrochemical measurement

Fabrication of NCM523 electrodes and coin cells: A mixture of 80% NCM523 materials (supplied by an industrial partner), 10% acetylene black and 10% polyvinylidene fluoride (PVDF) was uniformly dispersed into N–methyl-1, 2-pyrrolidone (NMP). Then the slurry was coated onto an Al foil using an automatic coating machine to get the NCM523 electrodes. After dried at 80 °C overnight in a vacuum oven, the NCM523 electrodes were punched into wafers. The area of the electrode is approximately 1.13 $cm^2$ and the amount of NCM523 loaded on the electrode is about 2.34 mg. The CR2016 coin cell was assembled with the NCM523 electrode, a separator (Celgard 2400), electrolyte (1 M $LiPF_6$, EC/DMC = 1:1 v/v) and the Li counter electrode in an argon-filled glove box.

Electrochemical charging/discharging test: The charging test consisted of a constant-current step at the voltage regions of 3.0–4.4 V, 3.0–4.5 V and 3.0–4.7 V under 75 mA $g^{-1}$ (0.5C, 1C = 150 mA $g^{-1}$) and a constant-voltage step at the upper-limit charging potential. The discharging test only consisted of a constant-current step under 0.5C. The NCM523 coin cells were measured at 25 °C by the LAND CT-2001A battery testing system. For the elevated temperature measurement, the operating temperature was increased to 60 °C after 50 charging/discharging cycles at 25 °C. The electrochemical impedance spectroscopy (EIS) measurements used the Solartron 1287/1260 electrochemical workstation at 25 °C in the frequency range of 100 kHz-0.01 Hz. The fully charged NCM523 coin cells were tested after 10 and 50 cycles under various voltage regions, respectively.

## 3. Results and discussion

The XRD data of the pristine NCM523 materials (Fig. S1a) shows a typical α-$NaFeO_2$-type rhombohedral layered structure belonging to the R-3m space group without any impurities. The clear peak splitting of the (006)/(102) and (108)/(110) peaks indicates a well-ordered layered structure [2,5,27]. In Fig. S1b, the NCM523 cathode materials are spherical secondary particles with an average diameter of 5 μm by SEM. The elemental composition of NCM523 measured by ICP-AES is Li: Ni: Co: Mn = 1.030: 0.518: 0.197: 0.285, which agrees well with the theoretical ratio value of NCM523.

The electrochemical performance tests of NCM523 are operated in the voltage regions of 3.0–4.4 V, 3.0–4.5 V and 3.0–4.7 V (0.5C), respectively. In Fig. 1, the specific discharge capacities of the first cycle in the voltage regions of 3.0–4.4 V, 3.0–4.5 V and 3.0–4.7 V (0.5C) are 178.0, 189.3 and 197.5 mAh·$g^{-1}$, which correspond to the area specific capacities of 0.3677, 0.3932 and 0.4111 mAh·$cm^{-2}$, respectively. This exhibits an enhancement of the initial specific discharge capacity comparing to that in the voltage region of 3.0–4.3 V (0.5C) in Fig. S1c. However, a significant phenomenon of capacity decay is observed during prolonged cycles. The capacity retention after 150 cycles decreases from 88.9% to 81.1% and 63.8% for the voltage region of 3.0–4.4 V, 3.0–4.5 V and 3.0–4.7 V (0.5C), respectively. The detailed test results of the cycling performance are listed in Tab. S1.

As reported by previous studies, Raman spectroscopy is an efficient tool to investigate the intrinsic state-of-charge (SOC) of NCM materials, because the local coordination structure is very sensitive to the Li amount of the material [28–31]. Fig. 2a presents the typical $A_{1g}$ (596 $cm^{-1}$) and $E_g$ (489 $cm^{-1}$) Raman peaks of the pristine NCM523 material, arising from the M − O (M = Ni, Co, Mn) stretching vibrations and the O-M-O bending vibrations, respectively [29,32,33]. To confirm the correlation between the Raman spectral features and the SOC of NCM523, Fig. 2a–b shows the Raman spectra of the NCM523 electrodes charged to different potentials (signed as 1c3.69 V, 1c3.79 V, 1c3.88 V, 1c3.93 V, 1c4.13 V, 1c4.21 V, 1c4.40 V, 1c4.50 V and 1c4.70 V) at 0.5C in the first cycle. With the de-intercalation of $Li^+$, the I ($A_{1g}$)/I ($E_g$) value decreases and a new peak at ~545 $cm^{-1}$ appears, which is attributed to the change in the M − O local environments caused by the oxidation

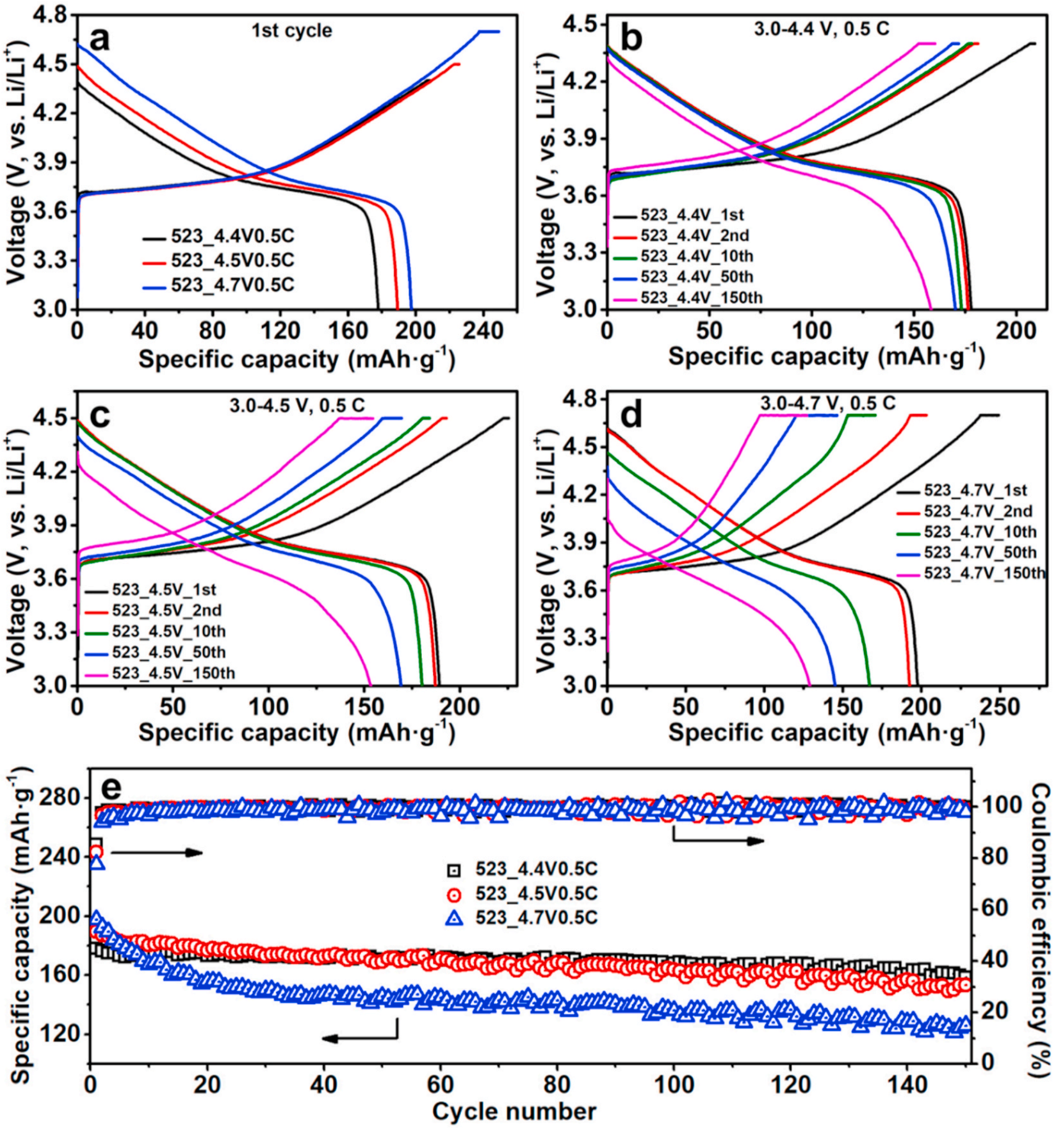

**Fig. 1.** The charging/discharging curves for the first cycle (a) and during 150 cycles (b–d) and the cycling performance (e) of NCM523 coin cells in the voltage regions of 3.0–4.4 V, 3.0–4.5 V and 3.0–4.7 V (0.5C).

reaction of $Ni^{2+}/Ni^{4+}$ during the charging process [28,34,35]. In addition, the slight downshift of the $E_g$ peaks from 489 $cm^{-1}$ to 478 $cm^{-1}$ may be caused by the lattice expansion in the c axis during the de-intercalation of $Li^+$ [29,36]. When discharging to 3.0 V for the samples cycling in different voltage regions (Fig. 2c–e), the Raman spectra gradually return to a state similar to the pristine state, which corresponds to the reduction reaction of $Ni^{4+}/Ni^{2+}$ during the discharging process. The detailed Raman spectra during the first discharging process are presented in Fig. S2. Therefore, in Fig. 2g–h, the correlation between the Raman spectral characteristics and the SOC of NCM523 is established based on the value of I $(A_{1g})$/I $(E_g)$ and I (545 $cm^{-1}$)/I $(E_g)$. The I $(A_{1g})$/I $(E_g)$ value monotonically increases with x at $0.4 < x < 1.0$; the I (545 $cm^{-1}$)/I $(E_g)$ value monotonically decreases with x at $0 < x < 0.4$. Simultaneously, the correlation between the Raman spectral characteristics and the SOC of NCM523 in the first cycle is nearly independent of the upper-limit charging potentials (Fig. 2h).

As mentioned above, the relative intensity of Raman spectral peaks can reflect the SOC of NCM523. Therefore, the changes in the SOC values of the cycled NCM523 electrodes can be estimated by the intensity ratios of Raman spectral peaks (I (545 $cm^{-1}$)/I $(E_g)$ and I $(A_{1g})$/I $(E_g)$) in Fig. 2g–h, as shown in Fig. S11. Fig. 3 shows the Raman spectra of the cycled NCM523 electrodes and their corresponding changes in the SOC value. In the first charging/discharging cycle in the voltage region of 3.0–4.4 V, only ~0.64 Li of the ~0.78 Li extracted during charging can re-intercalate into the structure during discharging. During the prolonged cycles, the I (545 $cm^{-1}$)/I $(E_g)$ value of the fully charged NCM523 electrodes stays unchanged. Therefore, ~0.22 Li always remains in the structure at the end of charge (Fig. 3a and g). However, the decreased I $(A_{1g})$/I $(E_g)$ value of the fully discharged NCM523 electrodes indicates an irreversible intercalation of $Li^+$ into the structure at the end of discharge (~3.7–3.0 V). Thus, the SOC value of the fully discharged NCM523 electrodes reduces from ~0.86 Li to less than ~0.80 Li (Fig. 3b and h). As a result, the SOC window in the voltage region of 3.0–4.4 V gradually narrows from 0.22 Li - 0.86 Li (the 1st cycle) to 0.22 Li - 0.80 Li (the 150th cycle). Although 0.84 Li and 0.93 Li can de-intercalate from the structure during charging to 4.5 V and 4.7 V in the first cycle, only 0.69 Li and 0.73 Li can re-intercalate into the structure after discharging to 3.0 V, indicating more capacity achievement but the lower coulombic efficiency under the higher upper-limit charging potential (Fig. 3g–h and Fig. S4). During long-term cycles in the voltage region of 3.0–4.5 V, the I (545 $cm^{-1}$)/I $(E_g)$ value of the fully charged NCM523 electrodes begins to decrease after 50 cycles, indicating a

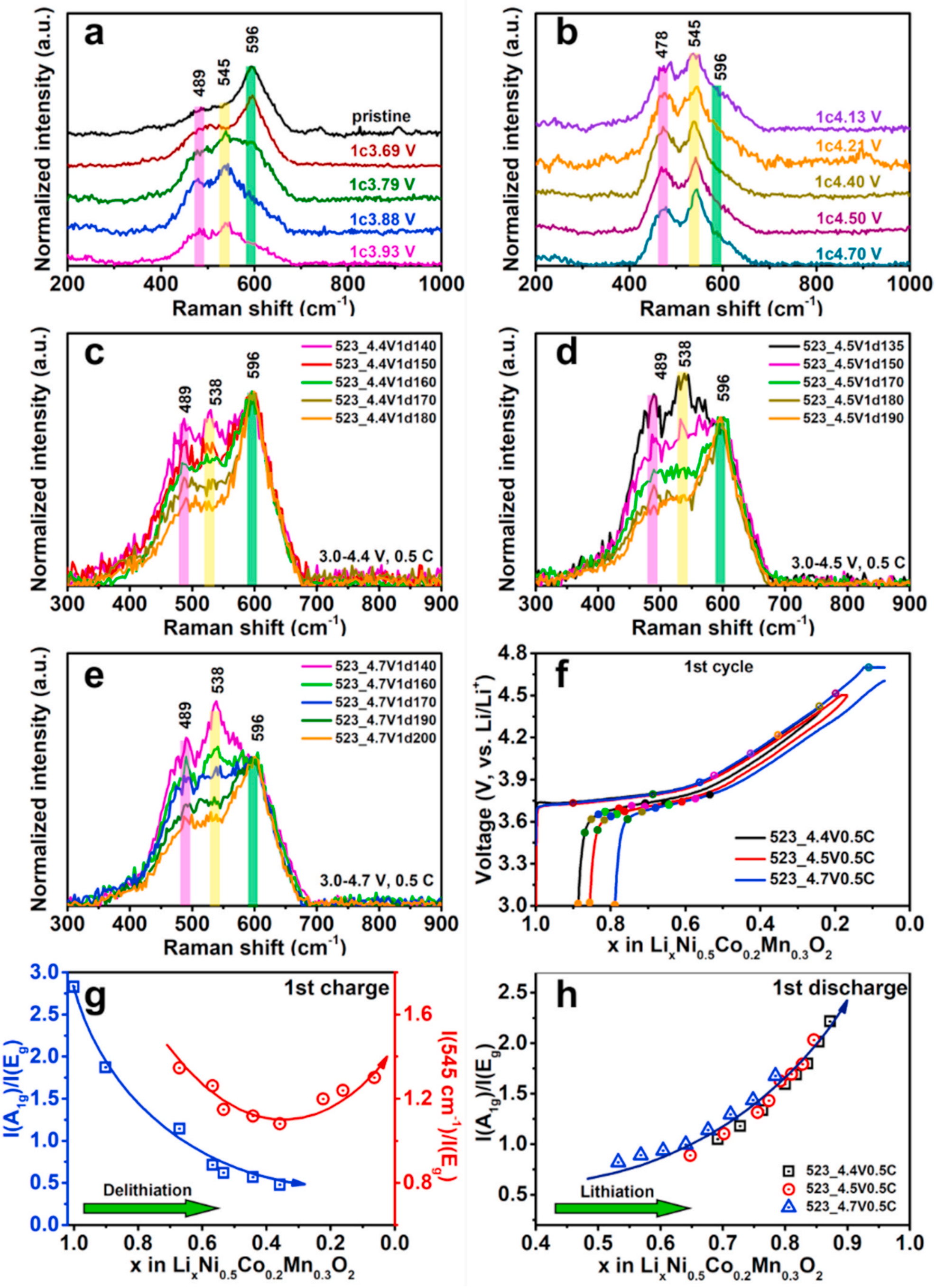

**Fig. 2.** The Raman spectra of the NCM523 electrodes charged to 4.7 V during the first charging process (a–b). The Raman spectra of the NCM523 electrodes discharged to the fixed specific capacity during the first discharging process in the voltage regions of 3.0–4.4 V (c), 3.0–4.5 V (d) and 3.0–4.7 V (e). The sample locations for the Raman spectral measurement indicated by the dots in the charging/discharging curves of NCM523 during the first cycle at different upper-limit charging potentials (f). The correlation curves between Raman spectral characteristics and the SOC of NCM523 during the first charging (g) and discharging (h) processes.

narrowed SOC window from 0.16 Li - 0.85 Li to 0.30 Li - 0.73 Li (Fig. 3c–d and Fig. 3g–h). In the voltage region of 3.0–4.7 V, the I (545 cm$^{-1}$)/I (E$_g$) value of the fully charged NCM523 electrodes and the I (A$_{1g}$)/I (E$_g$) value of the fully discharged NCM523 electrodes both decrease continuously since the first cycle (Fig. 3e–h), which indicates a narrowed SOC window from 0.07 Li - 0.80 Li to 0.33 Li - 0.73 Li.

Fig. 4a–c exhibit the capacity differential curves of NCM523 in the voltage regions of 3.0–4.4 V, 3.0–4.5 V and 3.0–4.7 V. The redox peaks around 3.74 V are associated with the redox reaction of Ni$^{2+}$/Ni$^{4+}$ [2, 11]. Obviously, the potential difference between the redox peaks increases with cycling, accompanied by a decreasing peak intensity and discharging potential, which indicates an increased electrode polarization, especially for the sample cycled in the voltage region of 3.0–4.7 V. The relative Li$^+$ diffusion coefficient tested by galvanostatic intermittent titration technique (GITT) is used to evaluate the effects of the upper-limit charging potential on the Li$^+$ diffusion kinetics in the bulk structure (Fig. S6) [4,37,38]. Noting that the relative Li$^+$ diffusion coefficient at the beginning of discharge in the voltage region of 3.0–4.7 V (Fig. 4f) is apparently higher than that of 3.0–4.4 V (Fig. 4d) or 3.0–4.5 V (Fig. 4e), which may be attributed to the larger concentration gradient between the bulk structure of NCM523 and the electrolyte caused by the higher delithiation degree at the end of charge at 3.0–4.7 V [39]. However, after cycling in the same voltage regions, no significant difference appears. It implies that the kinetics of Li$^+$ diffusion in the bulk structure seems not to be related with the increased electrode polarization after prolonged cycles. However, in Fig. 4g–h, the interfacial charge transfer resistance (R$_{ct}$, the medium-frequency semi-circle [3,40, 41]) measured by EIS increases distinctly after cycling, especially for the

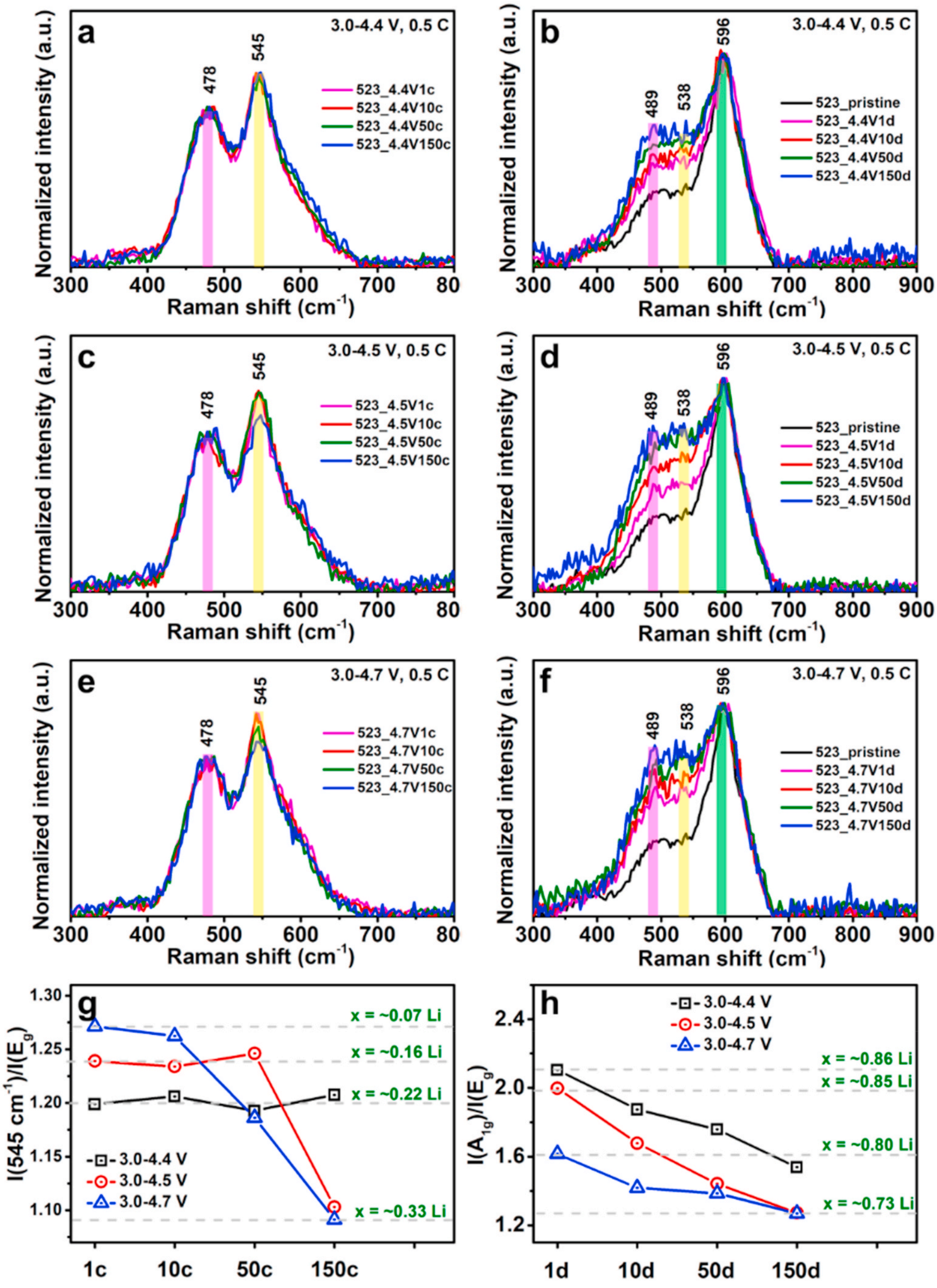

**Fig. 3.** The Raman spectra of the fully charged (a, c, e) and discharged (b, d, f) NCM523 electrodes after 1, 10, 50, 150 cycles in the voltage regions of 3.0–4.4 V, 3.0–4.5 V and 3.0–4.7 V. The changes in the I (545 cm$^{-1}$)/I ($E_g$) value of the fully charged NCM523 electrodes (g) and the I ($A_{1g}$)/I ($E_g$) value of the fully discharged NCM523 electrodes (h), the dotted lines represent the estimated SOC values.

sample cycled in the voltage region of 3.0–4.7 V. Consequently, according to the results in Figs. 3 and 4, it is suspected that the decay of the charging and discharging degree of NCM523 after long-term cycles under high upper-limit charging potentials can be attributed to the increased interfacial charge transfer resistance $R_{ct}$.

Furthermore, through a subsequent charging/discharging cycle at a lower current density (0.05C) after 150 cycles in the voltage regions of 3.0–4.4 V, 3.0–4.5 V and 3.0–4.7 V, the specific discharge capacity can be restored to 185.5, 182.3, 160.2 mAh·g$^{-1}$, respectively (Fig. 5a). The I ($A_{1g}$)/I ($E_g$) values of the corresponding Raman spectra also increase to a certain extent, which depends on the upper-limit charging potential (Fig. 5b–d and Fig. S7) and indicates that reducing the current density promotes more Li$^+$ to re-intercalate into the structure. Therefore, it can be concluded that the apparent capacity decay of NCM523 mainly originates from the retarding effect of the increased interfacial charge transfer resistance on Li$^+$ de-/intercalation during cycling under the high upper-limit charging potential.

Moreover, after 50 cycles in the voltage region of 3.0–4.7 V (0.5C), the specific discharge capacity decreases from 197.5 to ~153 mAh·g$^{-1}$. In Fig. 5e, the specific discharge capacity can be restored to 172.2, 177.1 and 167.7 mAh·g$^{-1}$ after a subsequent charging/discharging cycle at the lower current density (0.1C, 0.05C and 0.01C), respectively. The parasitic reaction at the electrode/electrolyte interface under the high potential may be aggravated at the extremely low current density of 0.01C,

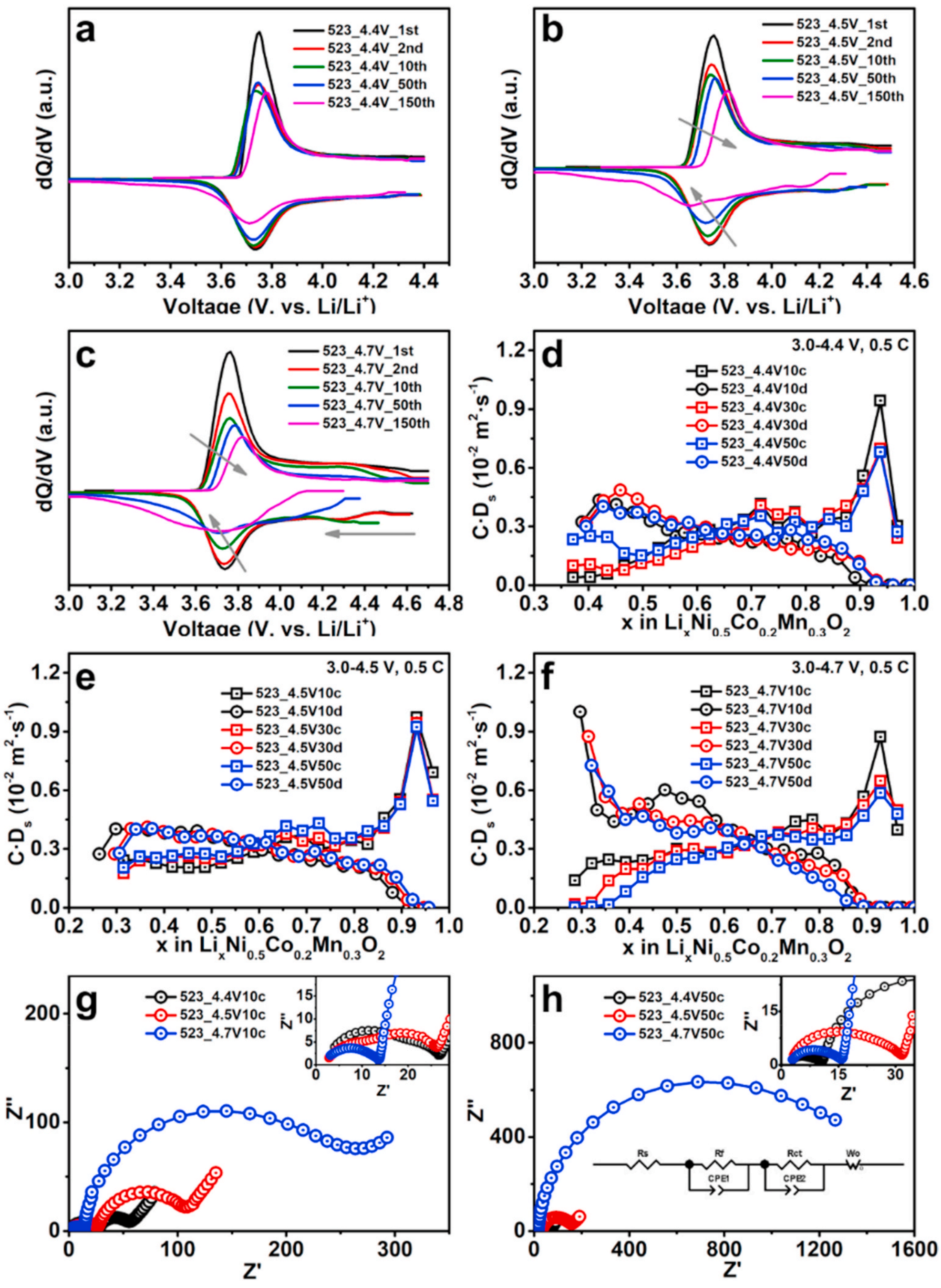

**Fig. 4.** The differential capacity curves of NCM523 coin cells during 150 cycles in the voltage regions of 3.0–4.4 V (a), 3.0–4.5 V (b) and 3–4.7 V (c).The relative $Li^+$ diffusion coefficients of NCM523 during the 10th, 30th and 50th cycles in the voltage regions of 3.0–4.4 V (d), 3.0–4.5 V (e) and 3.0–4.7 V (f). The EIS profiles of NCM523 after 10 cycles (g) and 50 cycles (h) at various upper-limit charging potentials. The inset shows the equivalent circuit of the NCM523 electrode. $R_{s:}$ solution resistance; $R_f$: surface film resistance; $R_{ct}$: interfacial charge transfer resistance; $W_o$: Warburg resistance.

causing the overcharge. Therefore, the current density of 0.05C is more suitable for the capacity recovery. Interestingly, the specific discharge capacity drops back to ~150 mAh·$g^{-1}$ after the current density returns to 0.5C, which confirms that the retarding effect exists objectively at 0.5C and the apparent capacity loss is indeed due to the kinetic degradation of $Li^+$ de-/intercalation. To figure out the influence of the retarding effect on the de-/intercalation of $Li^+$ respectively, the electrochemical charging/discharging measurements are performed as follows: i) After 100 cycles at 3.0–4.7 V (0.5C), the NCM523 coin cells are operated for five charging/discharging cycles at the "0.05 C-charge/ 0.05 C-discharge" step; ii) Then the NCM523 coin cells continue to be operated for one charging/discharging cycle at "0.5 C-charge/0.05 C-discharge" and "0.05 C-charge/0.5 C-discharge" steps, respectively. In Fig. 5f–g, the specific charge capacity decreases from 177.7 to 172.5 mAh·$g^{-1}$ when the charging current density rises from 0.05C to 0.5C, suggesting that a small amount of lithium ions fail to de-intercalate from NCM523 due to the retarding effect. However, the large discharge capacity loss (from 170.6 to 150.6 mAh·$g^{-1}$) points out that more lithium ions fail to re-intercalate into NCM523 after the discharge current density rises form 0.05C–0.5C. Therefore, it is supposed that the retarding effect on $Li^+$ intercalation is more remarkable than that on $Li^+$ de-intercalation, which explains the asymmetric phenomenon of the changes in the SOC of the fully charged/discharged NCM523 electrodes during long-term cycles. The constant-voltage charging step can provide extra driving force for $Li^+$ de-intercalation. Meanwhile, it is reported that the polarization of $Li^+$ intercalation is larger than that of $Li^+$ de-intercalation, which is derived from the slow $Li^+$ mobility due to the transition metal ions in the lithium layers [42]. In addition, in Fig. 5h, the long-cycle capacity loss can also be restored by increasing the operating temperature from 25 °C to 60 °C, which may be related with

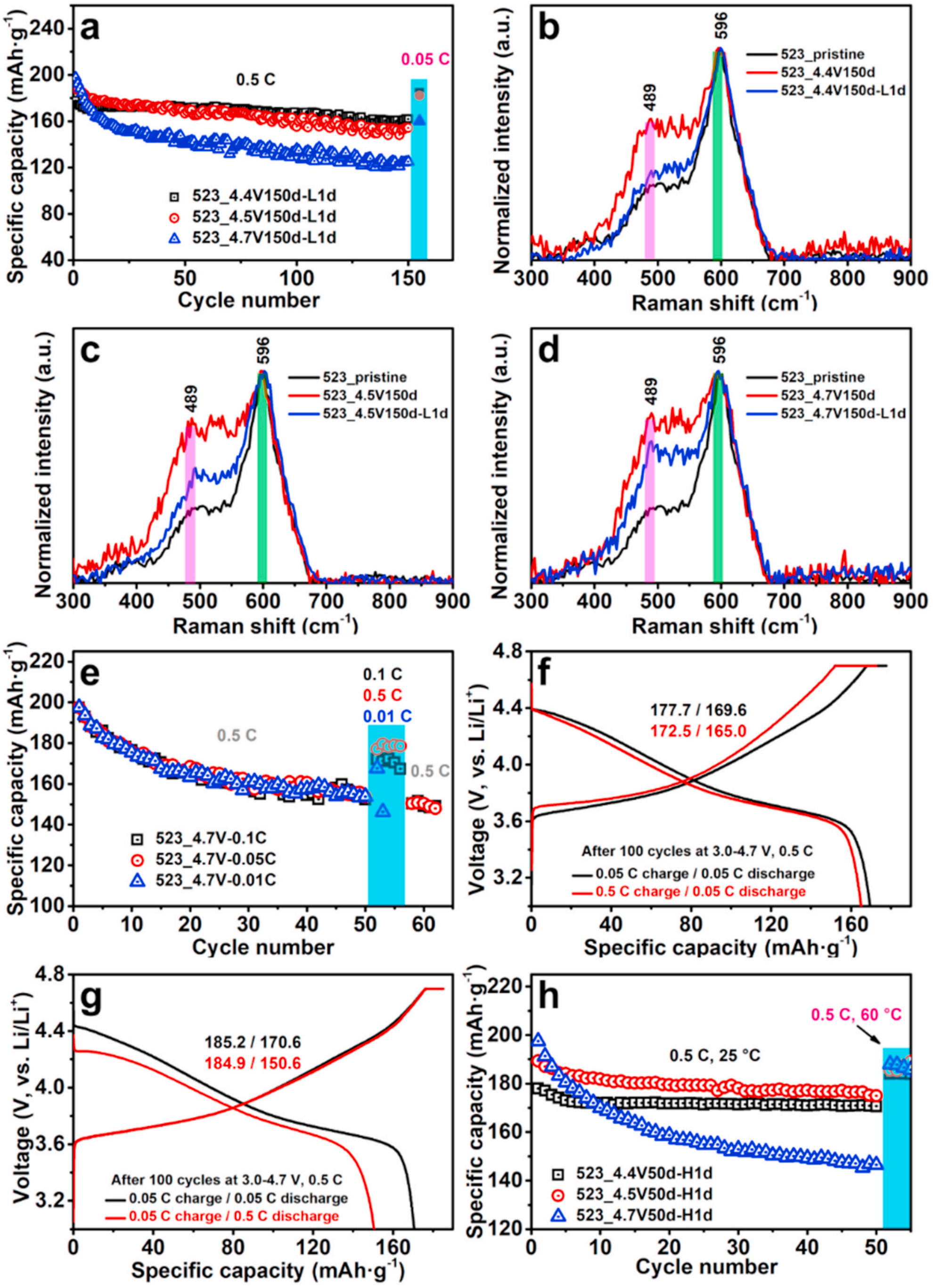

**Fig. 5.** The cycling performances (a) and Raman spectra (b–d) of NCM523 after 150 cycles and a subsequent charging/discharging cycle at a lower current density of 0.05C. The cycling performances of NCM523 after changing the current density in the voltage region of 3.0–4.7 V (e). The charging/discharging curves of NCM523 in one cycle at the "0.5 C-charge/0.05 C-discharge" (f) and "0.05 C-charge/0.5 C-discharge" (g) steps after long-term cycles in the voltage region of 3.0–4.7 V. The cycling performances of NCM523 after increasing the operating temperature from 25 °C to 60 °C at different upper-limit charging potential (h).

the acceleration of the Li$^{+}$ mobility under an increased operating temperature. In summary, the results above can attribute the apparent long-cycle capacity decay of high-voltage NCM523 to the increased retarding effect of the interfacial charge transfer resistance on Li$^{+}$ de-/intercalation. In particular, the retarding effect on Li$^{+}$ intercalation is more remarkable than that on Li$^{+}$ de-intercalation, and the NCM523 material cycling under the higher upper-limit charging potential will exhibit the more obvious retarding effect.

To further study the origin of the increased retarding effect on Li$^{+}$ de-/intercalation, the XRD, HR-TEM and XPS measurements are applied to characterize the bulk and surface structure, respectively. The XRD patterns of the fully discharged NCM523 electrodes after 50 cycles under different upper-limit charging potential are shown in Fig. 6. The $(311)_{Al}$ peak at 78.306° from the Al foil is used to correct the peak positions in the XRD patterns (Fig. 6e). All of the cycled NCM523 electrodes exhibit a typical α-$NaFeO_2$-type rhombohedral layered structure (Fig. 6a). The obvious separation of the (006)/(102) and (108)/(110) peaks (Fig. 6c–d) implies no distinguishable change in the bulk structure before and after cycling [27,43,44]. It is worth noting that the (003), (006) and (108) peak positions of all the cycled NCM523 electrodes shift to a lower degree, while the (102) peak positions shift slightly to a higher degree, especially for the 3.0–4.7 V sample (Fig. 6b–d). It is reported that the (003), (006) and (108) peak positions downshift continuously and the (102) peak position upshifts slightly during the initial charging, which is caused by the expansion of the c-axis and the slight contraction of the a/b-axis during delithiation [45–48]. This may indicate that Li$^{+}$ cannot re-intercalate into the structure sufficiently at the end of discharge, thus causing the change of the XRD peak positions mentioned above.

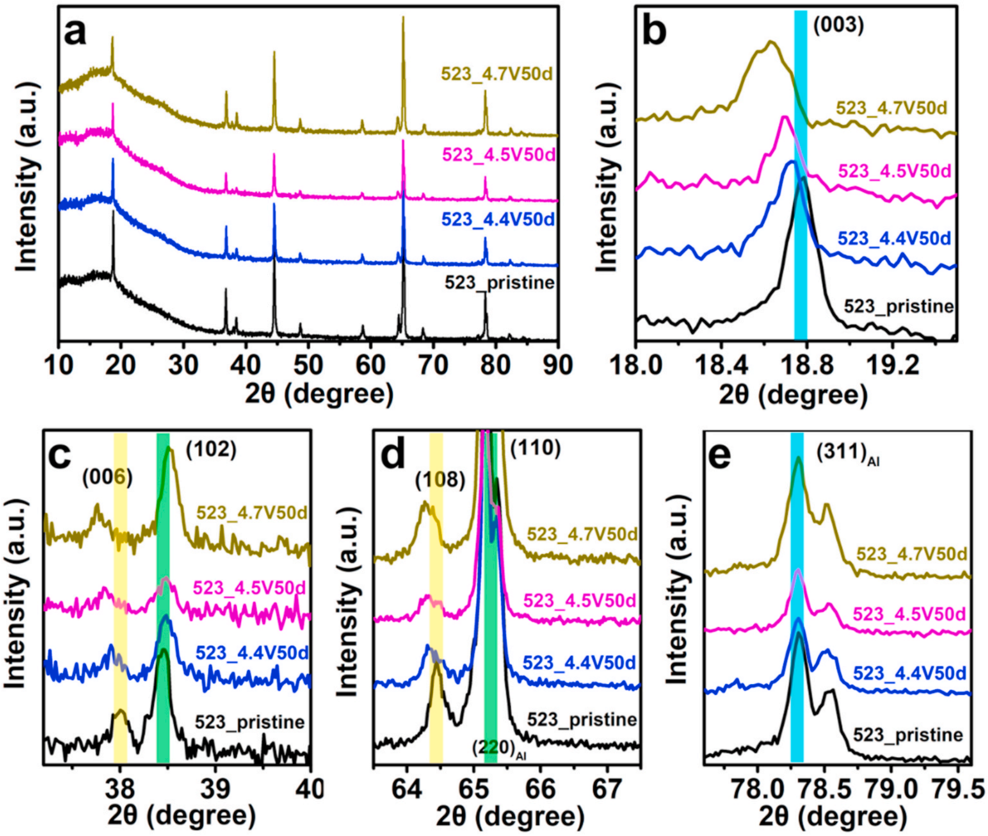

**Fig. 6.** The XRD patterns of the pristine and fully discharged NCM523 electrodes after 50 cycles in the voltage regions of 3.0–4.4 V, 3.0–4.5 V and 3.0–4.7 V.

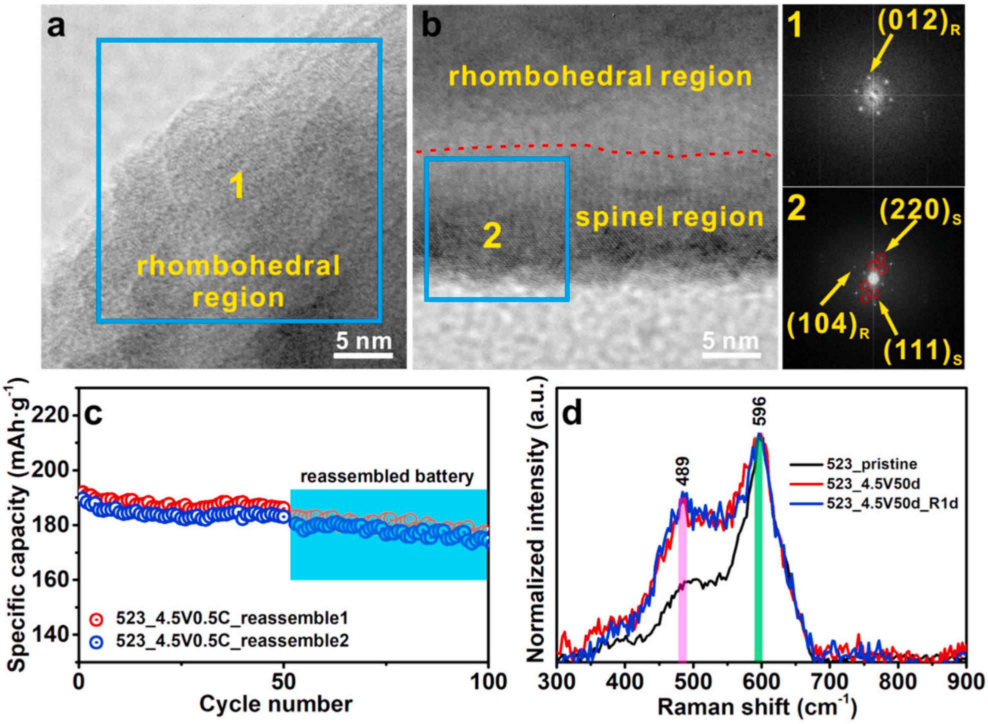

**Fig. 7.** The HR-TEM and FFT images of the pristine NCM523 sample (a) and the NCM523 sample after 100 cycles in the voltage region of 3.0–4.5 V (b). (R represents the layered structure, S represents the spinel structure.) The cycling performance tests (c) and the Raman spectra (d) of the reassembled NCM523 coin cell after 50 cycles in the voltage region of 3.0–4.5 V.

Meanwhile, as revealed by SEM in Fig. S10, there seems to be no distinct microcracks in the NCM523 particles after 50 cycles in all voltage regions, only a few microcracks appear after 150 cycles. Therefore, the consequences of the XRD, GITT and SEM measurements indicate that the bulk structure and the particle pulverization of NCM523 seems not to be closely related with the increased retarding effect during long cycles, which means the necessity of studying the electrode/electrolyte interface.

The surface structural evolution after cycling under high upper-limit charging potentials is revealed by the HR-TEM measurement. In Fig. 7a, both the surface and bulk structure of the pristine NCM523 show a consistent rhombohedral phase, belonging to the NCM layered structure (R-3m), as indicated by the Fast Fourier Transform (FFT) image of the region 1. After 100 cycles at 3.0–4.5 V, the spinel phase appears in the thickness of a dozen nanometers on the surface region (Fig. 7b), indicating that the surface structure of the NCM523 particles deteriorates continuously during cycling under the high upper-limit charging potential. The red circles in the FFT image of the region 2 correspond to the positions of the spinel structure (Fd-3m) [43]. Afterwards, the cycled NCM523 electrode is disassembled from the cycled coin cell and rinsed with DMC to remove the decomposition products of electrolyte. However, both of the capacity and the Raman spectral I ($A_{1g}$)/I ($E_g$) value of the NCM523 in the reassembled battery fails to recover under the same charge/discharge condition (Fig. 7c–d and Fig. S9), which means the decomposition products of electrolyte adsorbed on the surface of the NCM523 particles may not be closely related with the kinetic degradation of $Li^+$ de-/intercalation. Therefore, the surface structural deterioration of the NCM523 particles during long-term cycles may contribute prominently to the increased retarding effect. Due to the unstable highly-delithiated structure at the high potential, the surface structural deterioration is more serious under the higher upper-limit charging potential, thus making the retarding effect more obvious (Fig. S5) [13,14,43].

Furtherly, the XPS measurement is performed to characterize the surface species of NCM523 after long cycles, as presented in Fig. 8. For the Ni $2p_{3/2}$ spectra (Fig. 8a and e), the pristine NCM523 sample contains $Ni^{2+}$ (~854.5 eV) and $Ni^{3+}$ (~856.2 eV) [10,49–52]. After 100 cycles in the voltage region of 3.0–4.7 V, the content of $Ni^{3+}$ on the surface of the fully discharged NCM523 (signed as 4.7V100d) decreases significantly while the content of $Ni^{2+}$ and $NiF_2$ (~857.9 eV) increases. For the Co 2p spectra, it is usually difficult to assign the XPS peaks of Co 2p located at the binding energy of 780–784 eV (Fig. 8b) due to its complex components of the XPS peaks (i.e. Co $2p_{3/2}$ peaks, satellite peaks, Ni Auger peaks, $CoF_2$ peaks) [10,50]. For the Mn 2p spectra (Fig. 8c), the shift of the Mn $2p_{3/2}$ peak position to the low binding energy indicates the increased content of $Mn^{3+}/Mn^{2+}$ after prolonged cycles at 3.0–4.7 V [50]. Therefore, it obviously indicates a surface evolution of NCM523 after long cycles under the high upper-limit

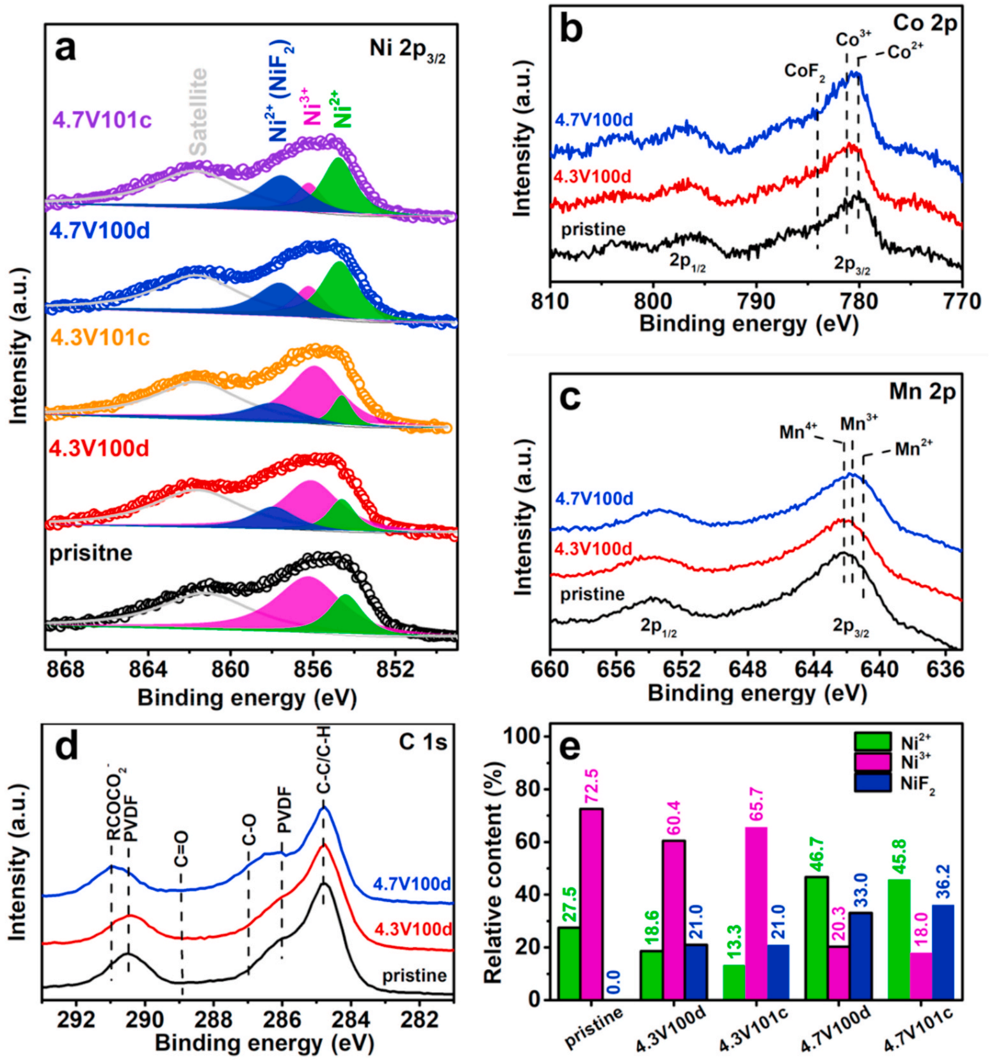

**Fig. 8.** The XPS spectral comparison in the surface elements of the pristine and cycled NCM523 electrodes in the voltage regions of 3.0–4.3 V and 3.0–4.7 V: Ni $2p_{3/2}$ (a), Co 2p (b), Mn 2p (c) and C 1s (d). The relative contents of $Ni^{2+}$, $Ni^{3+}$ and $NiF_2$ on the surface of the pristine and cycled NCM523 electrodes. (e).

charging potential. It is believed that the surface transition metal ions may be reduced in the form of oxide/fluoride, due to the unstable and highly-reactive $M^{4+}$-O (M = Ni, Co, Mn) bonds at the high potential [13,14,53]. The C 1s spectra (Fig. 8d) also prove that a large number of by-products (i.e. $RCOCO_2Li$) are produced on the surface of the cycled NCM523 electrodes, which can be attributed to the parasitic reaction at the electrode/electrolyte interface [9,41,49,51]. Furthermore, in Fig. 8a and e, after 100 cycles in the voltage region of 3.0–4.7 V, the Ni $2p_{3/2}$ spectrum of NCM523 in the fully discharged state (signed as 4.7V100d) exhibits nearly no difference from that in the fully charged state (signed as 4.7V101c), which may indicate an electrochemically passive surface layer of NCM523. However, after 100 cycles in the voltage region of 3.0–4.3 V, it still exhibits an electrochemically active surface layer of Ni, as indicated by the distinct difference between the Ni $2p_{3/2}$ spectra of NCM523 in the fully discharged state (signed as 4.3V100d) and the fully charged state (signed as 4.3V101c). Therefore, the HR-TEM and XPS measurements seem to indicate that an electrochemically passive layer would be formed on the material surface after long-term cycles under the high upper-limit charging potential. As reported by Bruce, the electrons move ahead of the ions in the electrode, which can generate an internal electrical field as the driving force to accelerate the motion of the ions [54]. Therefore, the electrochemical passivation layer formed on the material surface cannot be electrochemically polarized, so the internal electrical field in the material surface may be weakened, thus leading to a distinct increase in $R_{ct}$. In Fig. 4g–h. In most of the previous report, the $R_{ct}$ increase of NCM materials after long-term cycles under high upper-limit charging potentials was mainly attributed to the lattice mismatch between the layered structure and the spinel or rock salt phase [3,43,53,55,56]. However, the finding in our work provides another different possible mechanism about the $R_{ct}$ increase and the “capacity loss” of NCM materials, which is meaningful to improve the cycle stability of NCM materials during long-term cycles under high upper-limit charging potentials.

## 4. Conclusion

In this work, the mechanism of the apparent capacity decay of NCM523 during cycling at the high upper-limit charging potential (>4.3 V) is studied systematically from both the surface and bulk structure of NCM523. The results of Raman spectroscopy and the electrochemical measurements provide an important proof that the kinetic degradation of $Li^+$ de-/intercalation is a key factor for the apparent long-cycle capacity decay due to the increased interfacial charge transfer resistance. In particular, the retarding effect on $Li^+$ intercalation is more remarkable than that on $Li^+$ de-intercalation, and the NCM523 material cycling under the higher upper-limit charging potential will exhibit the more obvious retarding effect. Meanwhile, the apparent capacity loss can be significantly restored by reducing the current density or increasing the operating temperature. Furtherly, the XRD and GITT tests indicate a nearly unchanged bulk structure of NCM523 and bulk diffusion kinetics of $Li^+$ after cycling. However, the HR-TEM and XPS measurements indicate a passive surface layer formed after long-term cycles under the high upper-limit charging potential. Because the passive surface layer cannot be electrochemically polarized, the internal electrical field in the surface layer of the material may be weakened, which leads to the distinct increase in $R_{ct}$. Therefore, the electrochemical passivation of the surface structure of the NCM523 particles can be another important factor for the kinetic degradation of $Li^+$ de-/intercalation, besides the particle pulverization of NCM523 and the decomposition products of electrolyte adsorbed on the material surface reported in previous work. Therefore, this work will be helpful to deeply understand the intrinsic mechanism of the capacity decay of NCM523. Since the apparent capacity can be restored by reducing the current density or increasing the operating temperature, it exhibits instruction to help solving the urgent problems in practical applications, such as the cascade utilization of LIBs.

## CRediT authorship contribution statement

**Jiyang Li:** Conceptualization, Investigation, Funding acquisition, Data acquisition and Curation, Data curation, Writing – original draft. **Jingxin Huang:** Methodology, and Guidance, Writing-Review and Editing, Writing – review & editing. **Xiangbang Kong:** Data acquisition, Funding acquisition. **Jing Zeng:** Writing – review & editing, Writing-Review and Editing. **Jinbao Zhao:** Guidance and Supervision, Funding acquisition.

## Declaration of competing interest

The authors declare that they have no known competing financial interests or personal relationships that could have appeared to influence the work reported in this paper.

## Acknowledgement

We gratefully acknowledge the financial support of National Key Research and Development Program of China (2017YFB0102000), Fundamental Research Funds for the Central Universities (20720190040). The authors also want to express their gratitude to Dr. Chuan Liu and Dr. Dingliang Tang from College of Chemistry and Chemical Engineering in Xiamen University for their kind help on Raman spectroscopy measurements and XPS measurements.

## Appendix A. Supplementary data

Supplementary data to this article can be found online at https://doi.org/10.1016/j.jpowsour.2021.229856.

## References

[1] W. Li, A. Manthiram, Chem. Soc. Rev. 46 (2017) 3006–3059.

[2] Z. Chen, C. Liu, G. Sun, X. Kong, S. Lai, J. Li, R. Zhou, J. Wang, J. Zhao, ACS Appl. Mater. Interfaces 10 (2018) 25454–25464.

[3] X. Zhao, Q.-C. Zhuang, C. Wu, K. Wu, J.-M. Xu, M.-Y. Zhang, X.-L. Sun, J. Electrochem. Soc. 162 (2015) A2770–A2779.

[4] A. Verma, K. Smith, S. Santhanagopalan, D. Abraham, K.P. Yao, P.P. Mukherjee, J. Electrochem. Soc. 164 (2017) A3380–A3392.

[5] H.-J. Noh, S. Youn, C.S. Yoon, Y.-K. Sun, J. Power Sources 233 (2013) 121–130.

[6] H. Rong, W. Li, J. Power Sources 332 (2016) 312–321.

[7] P. Dong, T. Ren, J. Power Sources 344 (2017) 111–118.

[8] R. Zhou, J. Huang, S. Lai, J. Li, F. Wang, Z. Chen, W. Lin, C. Li, J. Wang, J. Zhao, Sustainable Energy & Fuels, 2018.

[9] P. Hong, W. Li, J. Electrochem. Soc. 164 (2016) A137–A144.

[10] D.-T. Nguyen, J. Kang, K.-M. Nam, Y. Paik, S.-W. Song, J. Power Sources 303 (2016) 150–158.

[11] L. Li, K. Zhang, J. Mater. Chem. A 3 (2015) 894–904.

[12] R.V. Chebiam, A.M. Kannan, F. Prado, A. Manthiram, Electrochem. Commun. 3 (2001) 624–627.

[13] H. Kuriyama, H. Saruwatari, H. Satake, A. Shima, F. Uesugi, H. Tanaka, T. Ushirogouchi, J. Power Sources 275 (2015) 99–105.

[14] M. Börner, F. Horsthemke, F. Kollmer, S. Haseloff, A. Friesen, P. Niehoff, S. Nowak, M. Winter, F.M. Schappacher, J. Power Sources 335 (2016) 45–55.

[15] H. Zheng, Q. Qu, G. Zhu, G. Liu, V.S. Battaglia, H. Zheng, ACS Appl. Mater. Interfaces 9 (2017) 12445–12452.

[16] K.-J. Park, J.-Y. Hwang, H.-H. Ryu, F. Maglia, S.-J. Kim, P. Lamp, C.S. Yoon, Y.-K. Sun, ACS Energy Letters (2019) 1394–1400.

[17] Y. Yu, P. Karayaylali, Y. Katayama, L. Giordano, M. Gauthier, F. Maglia, R. Jung, I. Lund, Y. Shao-Horn, J. Phys. Chem. C 122 (2018) 27368–27382.

[18] Y. Zhang, Y. Katayama, R. Tatara, L. Giordano, Y. Yu, D. Fraggedakis, J.G. Sun, F. Maglia, R. Jung, M.Z. Bazant, Y. Shao-Horn, Energy Environ. Sci. (2020).

[19] J.E. Harlow, X. Ma, J. Li, E. Logan, Y. Liu, N. Zhang, L. Ma, S.L. Glazier, M.M. E. Cormier, M. Genovese, S. Buteau, A. Cameron, J.E. Stark, J.R. Dahn, J. Electrochem. Soc. 166 (2019) A3031–A3044.

[20] L.M. Thompson, W. Stone, A. Eldesoky, N.K. Smith, C.R.M. McFarlane, J.S. Kim, M. B. Johnson, R. Petibon, J.R. Dahn, J. Electrochem. Soc. 165 (2018) A2732–A2740.

[21] J.A. Gilbert, I.A. Shkrob, D.P. Abraham, J. Electrochem. Soc. 164 (2017) A389–A399.

[22] J.R. Dahn, J. Electrochem. Soc. 164 (2017) A655–A665.

[23] J. Kasnatscheew, M. Evertz, B. Streipert, R. Wagner, R. Klopsch, B. Vortmann, H. Hahn, S. Nowak, M. Amereller, A.C. Gentschev, P. Lamp, M. Winter, Phys. Chem. Chem. Phys. : Phys. Chem. Chem. Phys. 18 (2016) 3956–3965.

[24] H. Zhou, F. Xin, B. Pei, M.S. Whittingham, ACS Energy Letters 4 (2019) 1902–1906.

[25] A. Grenier, P.J. Reeves, H. Liu, I.D. Seymour, K. Marker, K.M. Wiaderek, P. J. Chupas, C.P. Grey, K.W. Chapman, J. Am. Chem. Soc. 142 (2020) 7001–7011.

[26] R.E. Ruther, A.F. Callender, H. Zhou, S.K. Marth, J. Nanda, J. Electrochem. Soc. 162 (2015) A98–A102.

[27] Z. Chen, J. Wang, J. Huang, T. Fu, G. Sun, S. Lai, R. Zhou, K. Li, J. Zhao, J. Power Sources 363 (2017) 168–176.

[28] P. Lanz, C. Villevieille, P. Novák, Electrochim. Acta 130 (2014) 206–212.

[29] S. Fang, M. Yan, R.J. Hamers, J. Power Sources 352 (2017) 18–25.

[30] C. Ghanty, B. Markovsky, E.M. Erickson, M. Talianker, O. Haik, Y. Tal-Yossef, A. Mor, D. Aurbach, J. Lampert, A. Volkov, J.-Y. Shin, A. Garsuch, F.F. Chesneau, C. Erk, ChemElectroChem 2 (2015) 1479–1486.

[31] E. Flores, P. Novák, U. Aschauer, E.J. Berg, Chem. Mater. 32 (2019) 186–194.

[32] K. Ben-Kamel, N. Amdouni, A. Mauger, C.M. Julien, J. Alloys Compd. 528 (2012) 91–98.

[33] X. Zhang, A. Mauger, Q. Lu, H. Groult, L. Perrigaud, F. Gendron, C.M. Julien, Electrochim. Acta 55 (2010) 6440–6449.

[34] G. Singh, W.C. West, J. Soler, R.S. Katiyar, J. Power Sources 218 (2012) 34–38.

[35] M.-H. Lin, J.-H. Cheng, H.-F. Huang, U.-F. Chen, C.-M. Huang, H.-W. Hsieh, J.-M. Lee, J.-M. Chen, W.-N. Su, B.-J. Hwang, J. Power Sources 359 (2017) 539–548.

[36] E. Flores, U. Aschauer, E.J. Berg, Chem. Mater. 30 (2018) 4694–4703.

[37] Z. Mao, Z. Chen, Electrochim. Acta 222 (2016) 1741–1750.

[38] D.W. Dees, S. Kawauchi, D.P. Abraham, J. Prakash, J. Power Sources 189 (2009) 263–268.

[39] C. Hong, Q. Leng, J. Zhu, S. Zheng, H. He, Y. Li, R. Liu, J. Wan, Y. Yang, J. Mater. Chem. 8 (2020) 8540–8547.

[40] G.-L. Xu, Q. Liu, K.K.S. Lau, Y. Liu, X. Liu, H. Gao, X. Zhou, M. Zhuang, Y. Ren, J. Li, M. Shao, M. Ouyang, F. Pan, Z. Chen, K. Amine, G. Chen, Nature Energy 4 (2019) 484–494.

[41] Y. Chen, W. Zhao, Q. Zhang, G. Yang, J. Zheng, W. Tang, Q. Xu, C. Lai, J. Yang, C. Peng, Advanced Functional Materials, 2020.

[42] Y. Makimura, T. Sasaki, T. Nonaka, Y.F. Nishimura, T. Uyama, C. Okuda, Y. Itou, Y. Takeuchi, J. Mater. Chem. 4 (2016) 8350–8358.

[43] S.-K. Jung, H. Gwon, J. Hong, K.-Y. Park, D.-H. Seo, H. Kim, J. Hyun, W. Yang, K. Kang, Advanced Energy Materials 4 (2014) 1300787.

[44] X. Zhang, W.J. Jiang, X.P. Zhu, A. Mauger, Qilu, C.M. Julien, J. Power Sources 196 (2011) 5102–5108.

[45] S. Lee, D. Jang, J. Yoon, Y.-H. Cho, Y.-S. Lee, D.-H. Kim, W.-S. Kim, W.-S. Yoon, Journal of Electrochemical Science and Technology 3 (2012) 29–34.

[46] S. Zheng, C. Hong, X. Guan, Y. Xiang, X. Liu, G.-L. Xu, R. Liu, G. Zhong, F. Zheng, Y. Li, X. Zhang, Y. Ren, Z. Chen, K. Amine, Y. Yang, J. Power Sources 412 (2019) 336–343.

[47] W. Li, J.N. Reimers, J.R. Dahn, Solid State Ionics 67 (1993) 123–130.

[48] C.H. Shen, S.G. Sun, ACS Appl. Mater. Interfaces 8 (2016) 35323–35335.

[49] P. Hou, H. Zhang, X. Deng, X. Xu, L. Zhang, ACS Appl. Mater. Interfaces 9 (2017) 29643–29653.

[50] Y.-M. Lee, K.-M. Nam, E.-H. Hwang, Y.-G. Kwon, D.-H. Kang, S.-S. Kim, S.-W. Song, J. Phys. Chem. C 118 (2014) 10631–10639.

[51] Y. Han, S. Heng, Y. Wang, Q. Qu, H. Zheng, ACS Energy Letters (2020) 2421–2433.

[52] C. Wang, L. Shao, X. Guo, X. Xi, L. Yang, C. Huang, C. Zhou, H. Zhao, D. Yin, Z. Wang, ACS Appl. Mater. Interfaces 11 (2019) 44036–44045.

[53] F. Lin, I.M. Markus, D. Nordlund, T.-C. Weng, M.D. Asta, H.L. Xin, M.M. Doeff, Nat. Commun. 5 (2014) 3529.

[54] P.G. Bruce, Solid State Electrochemistry, Cambridge university press, 1995, pp. 203–216.

[55] L. Liang, X. Sun, C. Wu, L. Hou, J. Sun, X. Zhang, C. Yuan, ACS Appl. Mater. Interfaces 10 (2018) 5498–5510.

[56] A. Yano, Z. Ogumi, J. Electrochem. Soc. 162 (2015) A3137–A3144.